ORIGINAL PAPER

Corrosion Monitoring Assessment on Lithium Nitrate Molten Salts as Thermal Energy Storage Material Applied to CSP Plants

Abdiel Mallco[1,2] · Angel G. Fernández[1]

Abstract

The development of the new generation of concentrated solar power (CSP) plants requires improvements in the thermal energy storage systems, and corrosion produced is one of the main challenges to control since this can affect the costs of the electrical generation. Electrochemical impedance spectroscopy (EIS) has been applied in this research as a corrosion monitoring technique, comparing the results with conventional gravimetric corrosion tests. Gravimetric and electrochemical tests were conducted using AISI 304 stainless steel immersed in a ternary salt mixture composed of 57 wt% KNO_3 + 13 wt% $NaNO_3$ + 30 wt% $LiNO_3$ at 550 °C for 1000 h. The corrosion rate obtained using gravimetric and electrochemical tests was 7.8 μm/year and 5.7 μm/year, respectively. According to the results obtained in this research, EIS techniques could be a feasible option to control corrosion in CSP plants and reduce operational risks during the molten salt thermal-electricity conversion.

Keywords Thermal energy storage · Electrochemical impedance spectroscopy · Corrosion monitoring · Lithium nitrate · Concentrated solar power

Introduction

Over the last few years, renewable energies have become widespread throughout the world. This has allowed different technologies to play an important role in applied research [1]. In this sense, most of the applications related to the use of solar energy have been studied and analyzed depending on the type of application and technology [2].

✉ Angel G. Fernández
   angel.fernandez@uantof.cl

1   Centro de Desarrollo Energético de Antofagasta, Universidad de Antofagasta, Av. Universidad de Antofagasta, 02800 Antofagasta, Chile

2   Departamento de Ingeniería Mecánica, Universidad de Antofagasta, Av. Universidad de Antofagasta, 02800 Antofagasta, Chile

In this direction, concentrated solar power (CSP) technology concentrates and stores solar energy in the form of heat, using low-cost materials that are chemically stable over decades of use. Thus, CSP with thermal energy storage (TES) leads to an efficient package in the supply of renewable energy and, at the same time, provides significant capacity, reliability and dispatchability to the electricity grid, allowing a further increase in the use of this technology in electricity generation through renewable source systems [3–5].

Molten salts have been applied as heat transfer fluid (HTF) in concentrated solar power (CSP) plants [6], reaching excellent results in conventional power generation plants. The use of molten salts such as HTF and thermal storage material at the same time has allowed the proper use in the adaptation of different typical components of a thermal plant as heat exchangers, so that their use makes the solar field work at proper operating temperatures allowing the heat transfer fluids to fulfill the objective of transmitting the thermal energy to the rest of the system. However, molten salts solidify at relatively high temperatures, such is the case of solar salt where its solidification temperature is 220 °C [7, 8]. This means that special care must be taken to ensure that the molten salt does not solidify in the solar field pipes during certain times. Therefore, the routine operation of protection against the solidification of the molten salt should be carried out through different pieces of external equipment such as electrical resistance and electrical tracing that allow the optimal operation of a solar thermal plant with a molten salt storage system [9–11].

The fluid that is currently used as TES material in commercial CSP plants is a binary mixture composed of 60 wt% $NaNO_3$–40 wt% KNO_3 (solar salt), which has allowed the construction of several commercial plants that can store up to 15 h of energy [12, 13]. Among the most important characteristics and properties that should be emphasized in a TES fluid with the potential to be used as a heat storage material are density, specific heat, viscosity, thermal stability, among others. Henriquez et al. [14] proposed a ternary mixture of nitrates with a composition of 30%$LiNO_3$–13%$NaNO_3$–57%KNO_3 (% in weight, respectively); this mixture allowed excellent working ranges and outstanding thermal properties with respect to the solar salt. Bradshaw et al. [15] were among the first authors to report on $LiNO_3$, highlighting its adequate characteristics to improve the operating temperature range, although the main problem associated with lithium nitrate is its price. In fact, lithium nitrate is more expensive than potassium, calcium and sodium nitrate, so the cost is one of the main reasons why lithium salts have not been used in any commercial application so far, as well as $AgNO_3$ and $CsNO_3$ nitrates. Wang et al. [16] established a eutectic composition of 25.9 wt% $LiNO_3$ + 20.6 wt% $NaNO_3$ + 54.1 wt% KNO_3 and concluded that the thermal stability depends only on $LiNO_3$ since this component later becomes unstable and thermally decomposes to form Li_2O and Li_2O_2, where the other two components remain unchanged. Olivares et al. [17] studied the thermal behavior of the mixture composed of 30 wt% $LiNO_3$ + 18 wt% $NaNO_3$ + 52 wt% KNO_3 using DSC/TGA and determined that the melting points obtained using different covering atmospheres such as argon, nitrogen and oxygen were 121 °C, 122 °C and 120 °C, respectively. Therefore, this parameter is not influenced by the covering atmosphere used. Mohammad et al. [18] determined the melting point of

the mixture of 29.63 wt% $LiNO_3$ + 13.23 wt% $NaNO_3$ + 57.14 wt% KNO_3 experimentally and through computer simulations obtained the values of 122.8 °C and 120.84 °C, respectively. According to the arguments mentioned, the ternary mixture 30 wt% $LiNO_3$ + 57 wt% KNO_3 + 13 wt% $NaNO_3$ presents excellent physicochemical properties. Table 1 shows a summary of the thermal properties of the lithium-containing ternary mixture compared with other mixtures used as thermal storage media.

However, one of the most important challenges to be achieved is related to corrosion mitigation at high temperature since it is one of the most important issues for materials selection, structural design and service life prediction of engineering parts exposed to molten salt environments.

Commonly used corrosion evaluation techniques involve mass gain or loss in the steel immersed in the corrosive environment, and in recent years, more efforts have been made on the development of electrochemical techniques. Electrochemical impedance spectroscopy (EIS) has gained popularity since it can be performed in situ, and also because it usually does not require any artificial acceleration of the corrosion process. In this direction, linear polarization resistance (LPR) is a simple technique to obtain Tafel curves and corrosion rates as well [19].

For thermal energy storage systems, EIS could be an interesting option to monitor corrosion in energy generation plants since the low intensity of excitation signal used, which causes minimal disruption in the electrochemical system state and reducing the error associated with the conventional gravimetric measurement processes [20–22]. Impedance spectra obtained by this method are adjusted to an electrical circuit of a combination of resistors and capacitors (equivalent circuits), in order to interpret the corrosion mechanisms [23].

Nyquist equivalent circuit models are used to estimate the polarization resistance from the impedance data [24]. The Nyquist plot represents the real part of the impedance on the abscissa and the imaginary part thereof on the ordinate axis, both at different frequencies [25]. The semicircle obtained in the parallel RC circuit is used at higher values of Z' and represents the total impedance (Z) of the Randles circuit as:

Table 1 Properties of fluids considered for the solar thermal industry [5, 14]

Fluid	Density (kg/m³)	Melting point (°C)	Stability limit (°C)	Specific heat (J/kg K)
Solar salt (60%$NaNO_3$ + 40%KNO_3)	1880	220	600	1500
HITEC (7%$NaNO_3$ + 53%KNO_3 + 40%KNO_2)	1720	142	535	1560
HITEC XL (7%$NaNO_3$ + 45%KNO_3 + 48%Ca(NO_3)$_2$)	1991	120	500	1440
Proposed salt contained in lithium (30%$LiNO_3$ + 57%KNO_3 + 13%$NaNO_3$)	1820	120	596	1732

$$Z = R_S + \cfrac{1}{\cfrac{1}{R_{ct}} + j\omega C_{dl}} \tag{1}$$

where R_s is the resistance of the solution, R_{ct} is the resistance to charge transfer, $j\omega$ is the imaginary radial frequency and C_{dl} is the capacitance of the double layer. Different authors [19, 26, 27] proposed equivalent circuits that match to the main corrosion processes obtained in a molten salt environment at high temperature (Fig. 1).

Zeng et al. [26] established that, if the slope of the line obtained at low frequencies is less than 1, a porous scale could be formed on the metal surface. This layer can be considered as a non-protective barrier in contact with molten salts, and, therefore, the direction of diffusion into the alkaline cations is important in the corrosion behavior of different materials in contact with molten nitrates. In this case, the modulus of the Warburg resistance, related to the solubility and oxidants diffusion coefficient in the melt, should be considered [24].

The aim of this paper is the proposal of a corrosion monitoring technique to control corrosion processes in CSP storage tank using molten salts. For this purpose, corrosion rate comparison using both techniques (EIS and gravimetric studies) has been performed during 1000 h of immersion of a conventional stainless steel (AISI 304) in 30 wt% $LiNO_3$–13 wt% $NaNO_3$–57 wt% KNO_3 molten salt.
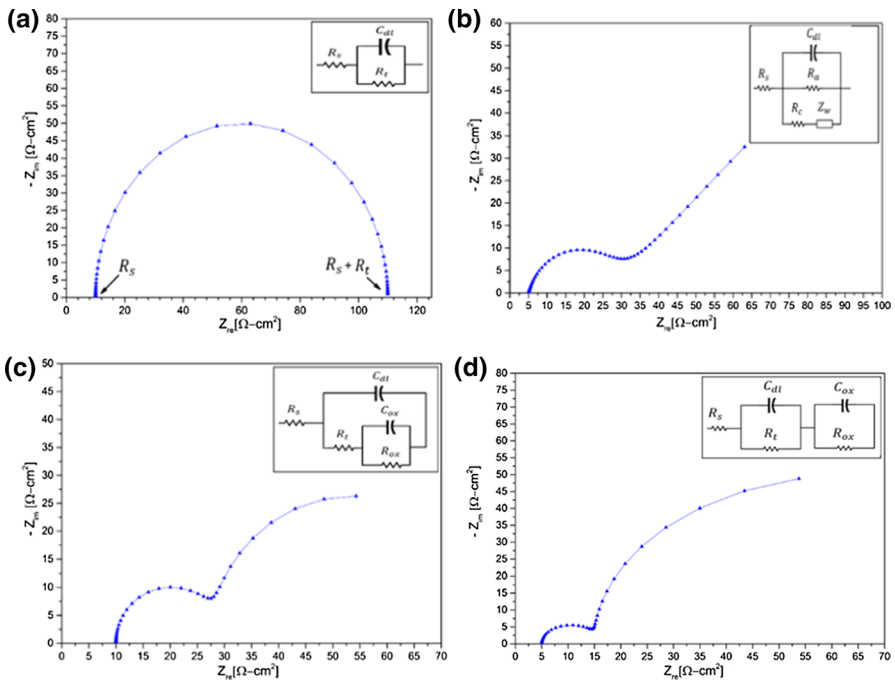

Fig. 1 Nyquist plots and the equivalent circuits representing the corrosion of metals in molten salts. **a** Representation of a non-active metal; **b** active metals forming a porous scale; **c** active metals forming a protective scale; and **d** active metals suffering from localized corrosion. (Adapted from [26])

Experimental Procedures

For this research, KNO_3 (99.5% purity) and $NaNO_3$ (99.5% purity), both acquired from Merck Company (Merck KGaA, Darmstadt, HD, Germany), and $LiNO_3$ (99% purity), acquired from Todini Company (Todini & Co SpA, Milano, Ml, Italy), formed our molten salt base for the lithium-containing ternary mixture. For the proper performance of static immersion test, the salt mixture (30 wt% $LiNO_3$–13 wt% $NaNO_3$–57 wt% KNO_3) was first introduced into the alumina crucibles in a furnace at different heating temperatures of 100, 200, 350 and 550 °C for 3 h in each case of temperature, reducing the impurity content of the salt mixtures and contributing to the dehydration of the salts [28, 29]. Once the salt mixture reached the temperature of 550 °C, this temperature was maintained for a whole day, so that they could be continuously homogenized and stabilized for the corresponding tests.

The corrosion test was implemented with isothermal gravimetric technique at 550 °C for 1000 h, retrieving samples after 200, 499, 699, 800 and 1000 h. The dimensions of each coupon, $20 \times 10 \times 2 \ mm^3$, were verified prior to the static immersion test using an electronic caliper to determine the surface areas of samples which were cleaned and degreased in water at 70 °C followed by distilled water and acetone and finally dried. The samples were polished with different abrasive papers progressively (SiC, P120, P600, P1200).

AISI 304 steel was selected for the different tests of this investigation, because it represents a commercial solution suitable for the case of the hot storage tank of CSP plants. The chemical composition of AISI 304 stainless steel is shown in Table 2.

The samples used for the static immersion test were quantified by the kinetics of net weight change carried out in different time intervals where each sample was exposed to measurement in 200, 400, 600, 800 and 1000 h of exposure. After completing the 1000 h of exposure, the samples were removed from the molten salt, slowly cooled and cleaned with hot distilled water.

Morphology and elemental composition of the exposed surfaces and their cross sections were inspected by SEM, model JEOL JSM-7500F, coupled to energy-dispersive X-ray spectrometer (EDS). The top surfaces of the analysis were treated properly. For cross section studies, coupons were mounted in a polymer resin prepared by mixing Remet Hardrock 554 resin and the hardener catalyst, in 2:1 proportion. After the resin cured (24 h at room temperature), the samples were ground and polished for a proper preparation.

The analysis of the crystallographic phase was determined by X-ray diffraction using a PANalytical X'Pert Pro and powder diffraction database.

Table 2 Chemical composition of stainless steel AISI 304

Stainless steel	wt%								
	Si	Mn	Cr	P	Mo	C	S	Ni	Fe
AISI 304	0.75 max	2 max	18–20	0.045 max	–	0.08 max	0.03 max	8–10.5	Balance

The samples used in the electrochemical impedance spectroscopy (EIS) and linear polarization resistance (LPR) tests were welded to a Fe–Cr–Al wire using the TIG (tungsten inert gas) welding technique. This is because it is necessary to establish a system that can conduct the electrical information to the electro-chemical test equipment, with a pulse current of 40 A, base current of 15 A and a frequency of 3 Hz. The working electrode (WE) and the counter electrode (CE) samples were introduced into a 5-mm-diameter alumina tube and sealed with high-temperature castable cement. The pseudo-electrode of reference (RE) was auto-circuited with the counter electrode (CE) for the electrochemical tests with the potentiostat (AUTOLAB-PGSTAT302N). Figure 2 shows the scheme of the electrochemical experimental setup.

Working electrode (WE) and reference–counter (RE–CE) electrodes were immersed in the molten salt (electrolyte), and the open-circuit potential (OCP) was measured using a potentiostat (AUTOLAB-PGSTAT302N). The values of the parameters for the electrochemical impedance test were obtained in a frequency range between 100 KHz and 10 MHz. Polarization tests were carried out between the potentials of −0.6 and 0.4 V of the OCP voltage (open-circuit potential). The scanning range is 0.001 V/s with steps of 0.00244 V.
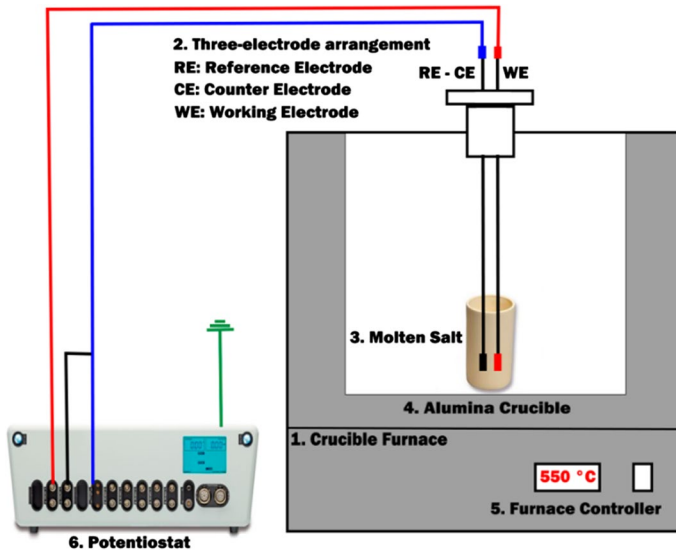

Fig. 2 Schematic of the electrochemical system: 1: muffle furnace; 2: three-electrode arrangement (*Re* reference electrode, *CE* counter electrode, *WE* working electrode or sample); 3: molten salt; 4: alumina crucible; 5: furnace controller; and 6: potentiostat

Results and Discussion

Gravimetric Test

Since AISI 304 stainless steel is presented as a suitable material in the different constructive systems of a thermal storage plant for mixing salts with nitrates at high temperature [14, 30–32], it is necessary to perform corrosion tests by static immersion test so that the effect of ternary mixing in lithium content can be evaluated in the material. In this case, corrosion tests are performed at 550 °C and 1000 h of exposure, where the kinetics of net weight change of AISI 304 is shown in Fig. 3.

The increase in mass gain after 400 h of exposure may be related to different phenomena that overlap in time, such as the formation of an oxide layer or the loss of mass after 800 h, that may be related to the dissolution of other layers formed on the surface of the material.

To complement the results of static immersion test of the stainless steel AISI 304 in the corrosive medium of ternary salt (LiNaK)NO_3, the surface study was carried out by scanning electron microscopy (SEM) as shown in Fig. 4. These results show a sustained growth in specific areas of the material forming a uniform layer of oxide as well as a spalled region due to the difference in the coefficients of thermal expansion between the oxides formed on the surface and what leads to the generation of layers on the surface of the sample; however, the protective effect on the entire layer is maintained.

The corrosion rate obtained from the static immersion test was obtained from the mass gain of the sample after 1000 h of exposure of the AISI 304 stainless steel, taking into account the density of the sample and the immersion time, obtaining a value of 7.8 μm/year. It is necessary to clarify that this result obtained refers to a corrosion rate
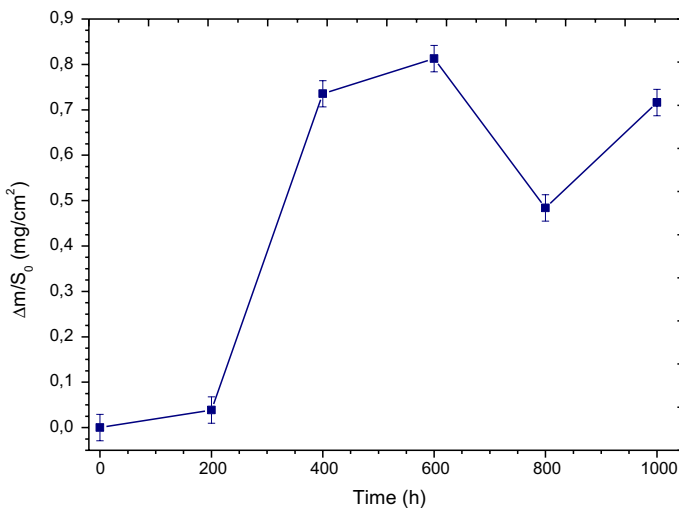

Fig. 3 Net weight change kinetics of AISI 304 stainless steel, exposure to molten salt (LiNaKNO_3) at 550 °C for 200, 400, 600, 800 and 1000 h
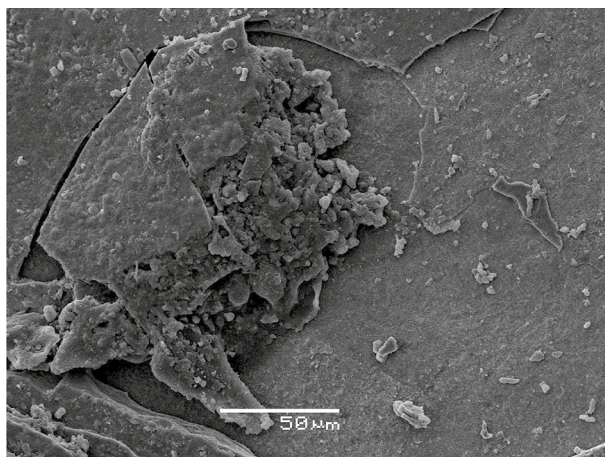
Fig. 4 SEM micrographs of top surface of AISI 304 at 800 h of immersion

for 1000 h of immersion where the results obtained for the static test with respect to electrochemical tests are merely comparative.

Electrochemical Impedance Spectroscopy Tests

Nyquist plots and their respective equivalent circuits are matching for a protective layer (Fig. 5) model for AISI 304 for 1000 h of test. The results of each electrochemical element are shown in Table 3.

Figure 5 shows the impedance spectra obtained for 304 stainless steel in contact with the LiNO$_3$ ternary salt at different exposure times. In all stages of the impedance measurement process, the formation of a protective layer is observed according to the corrosion models for molten salts available in the literature [26, 33]. These models are composed of two parallel circuits of resistors and capacitors connected in series to another resistor, in addition to a complex resistor called Warburg.

In this case, the corrosion layer formed is controlled by the transport of ions, and during the first hours of immersion, charge transfer reactions occur easily without limiting factor regarding corrosion rates. In contrast, at higher exposure times, the transport of ions and the diffusion of oxidants in the protective layer become a limiting process, which also depends on the protection formed in the metal. This diffusion of the oxidants is explained by incorporating in the protective layer equivalent circuit the resistance of Warburg Z_w, which can be interpreted as a reaction of oxidants-controlled diffusion in the molten salts. The Warburg resistance Z_w may be expressed by Eq. (2):

$$Z_w = W(jw)^{N_w} \tag{2}$$

where W is the modulus of Warburg resistance associated with the solubility and diffusion coefficient of oxidants in the molten salt and N_w is the Warburg coefficient that is related to the diffusion of oxidants.
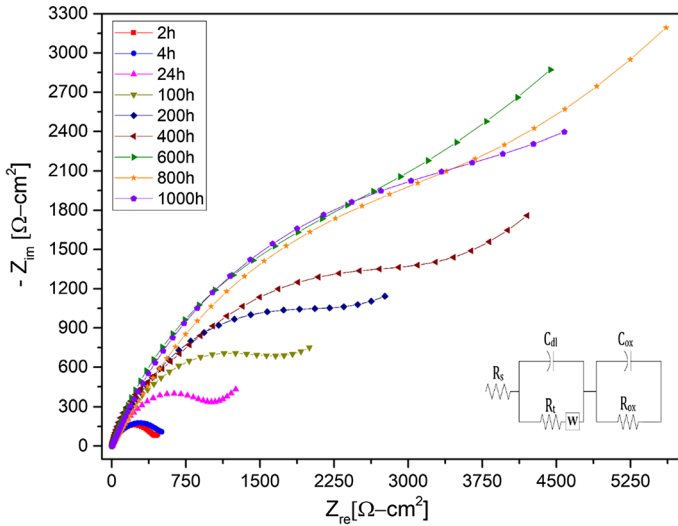
Fig. 5 Nyquist diagram of stainless steel 304 layer in KLiNaNO$_3$ for 0 h, 24 h, 100 h, 200 h, 400 h, 600 h, 800 h and 1000 h

Table 3 Fitting results of the impedance spectra of stainless steel 304 during corrosion in the presence of KLiNaNO$_3$ at 550 °C

Time	R_s	C_{dl}	β_{dl}	R_t	W	C_{ox}	β_{ox}	R_{ox}
Units	Ω cm^2	F s$^{(\beta_{dl}-1)}$		Ω cm^2	Ω s$^{-(1/2)}$	F s$^{(\beta_{ox}-1)}$		Ω cm^2
2 h	2.151	0.05	0.98	8.1	15	0.002	0.79	410
24 h	2.183	0.003	0.96	250.2	19	0.001	0.85	200
100 h	2.234	0.001	0.99	100.4	98	0.0015	0.76	1490
200 h	2.881	0.0007	0.91	410.7	140	0.0016	0.79	1950
400 h	3.152	0.0015	0.81	2900	150	0.00061	0.86	800
600 h	3.988	0.0016	0.99	2500	120	0.0018	0.69	5306
800 h	4.671	0.0005	0.98	2500	220	0.0002	0.65	2400
1000 h	4.718	0.0006	0.84	2800	180	0.0030	0.81	3200

The scale is considered as a capacitor since it is related to the double-layer capacitance at the steel/salt interface, represented by the equivalent circuit of Fig. 6, where C_{ox} represents the oxide capacitance and R_{ox} the transfer resistance of ions in the scale.

The second loop at low frequencies is referred to the corrosion process controlled by ions transport in the material surface layer, where R_s represents the molten salt (electrolyte) resistance, R_t is the electrochemical transfer resistance or polarization resistance of the tested material and C_{dl} is the double layer at the metal/salt interface. In this case, R_s values (electrolyte resistance) are increasing

Fig. 6 Equivalent circuit representing the corrosion of metals forming a protective scale in molten salts
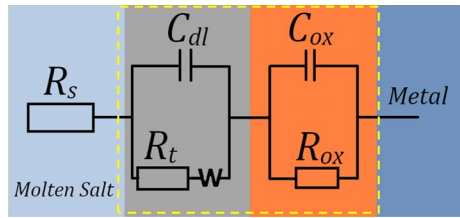
during the time (Table 3), so the electrical conductivity is reduced as well as the salt corrosiveness. Electrochemical impedance Z can be expressed by Eq. (3):

$$Z = R_{\mathrm{s}} + \frac{1}{jwC_{\mathrm{dl}} + wC_{\mathrm{dl}}\cot\left(\frac{\beta_{\mathrm{dl}}\pi}{2}\right) + \frac{1}{R_{\mathrm{t}}+Z_{\mathrm{w}}}} + \frac{1}{jwC_{\mathrm{ox}} + wC_{\mathrm{ox}}\cot\left(\frac{\beta_{\mathrm{ox}}\pi}{2}\right) + \frac{1}{R_{\mathrm{ox}}}} \quad (3)$$

where β_{dl} and β_{ox} represent the dispersion coefficient of the first and second capacitance of the circuit, respectively. Therefore, $wC_{\mathrm{dl}}\cot\left(\frac{\beta_{\mathrm{dl}}\pi}{2}\right)$ and $wC_{\mathrm{ox}}\cot\left(\frac{\beta_{\mathrm{ox}}\pi}{2}\right)$ are the elements of the impedance caused by the dispersion effect.

The corrosion mechanism obtained was fitted to a protective layer model during the isothermal immersion test. The Nyquist signals obtained at low frequency present higher impedance values, because it would correspond to a more homogenous formation of the protective layer in the metal. As it was mentioned before, the high-frequency semicircles correspond to the charge transfer reactions attached to the diffusion processes represented by the Warburg resistance.

Corrosion models were confirmed by scanning electron microscopy (SEM). These results are shown in Fig. 7, where a protective barrier composed of Fe–Cr–O was detected.

Complementarily, the results obtained through SEM–EDX and XRD (Fig. 8) show us objectively that the deposition of the different layers formed in the steels of study

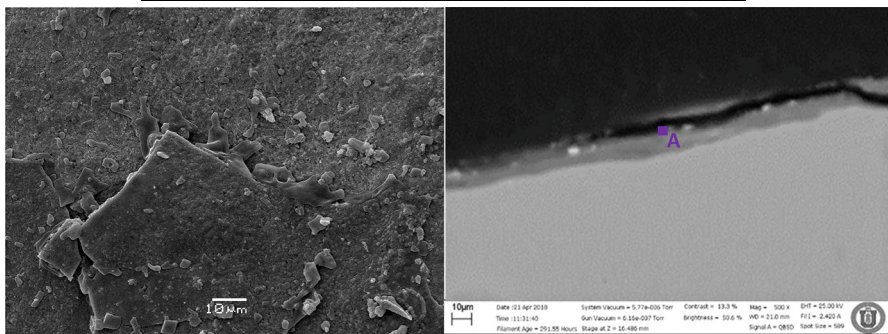| Analysis	O	Si	Cr	Mn	Fe	Ni	C
Spectrum A (% weigth)	28.53	0.33	6.49	0.57	23.95	2.18	37.95

Fig. 7 Surface (left) and cross section (right) image of stainless steel 304 in KLiNaNO$_3$ at 550 °C after 1000 h

of the electrochemical test has a character due to the processes of ion diffusion, fundamentally in the first hours of contact with the metal, which contributes to the need to monitor these stages and analyze the evolution of the corrosion process in molten salts. The oxidation caused by the effects of high temperature in different solar thermal storage materials generates the formation of different compounds, many of which can be inferred in some way based on the corrosion mechanisms in nitrates; we can find more stable compounds along the process, as well as the effect of lithium mainly (as a result of $LiNO_3$) and the other alkaline ions in the corrosion, due to the formation of other unstable compounds such as the iron–lithium compound oxide ($LiFeO_2$). Apart from the oxides identified as $FeCr_2O_4$ which form the inner layer of the protective layer, it is possible that $LiFeO_2$ can form a single layer, which in a way works as a corrosion inhibitor. It is necessary to understand better the function of lithium ion in this process, as it could have an application in other types of corrosive systems, so it is necessary to incorporate practical methods such as EIS, so that it can give us certain guidelines of the evolution of corrosion in systems as complex as molten salts [16, 34, 35].

Finally, in order to compare the corrosion rate obtained by gravimetric and electrochemical techniques, a linear polarization resistance test has been carried out by obtaining the Tafel curves shown in Fig. 9.

To quantify the polarization resistance R_p correctly from Eq. (5), it is important to take into account the potential drop attributed to the electrolyte resistance (molten salts). The relationship between polarization resistance and corrosion current density, i_{corr}, is expressed through Eq. (4):

$$i_{corr} = \frac{B}{R_p} \tag{4}$$

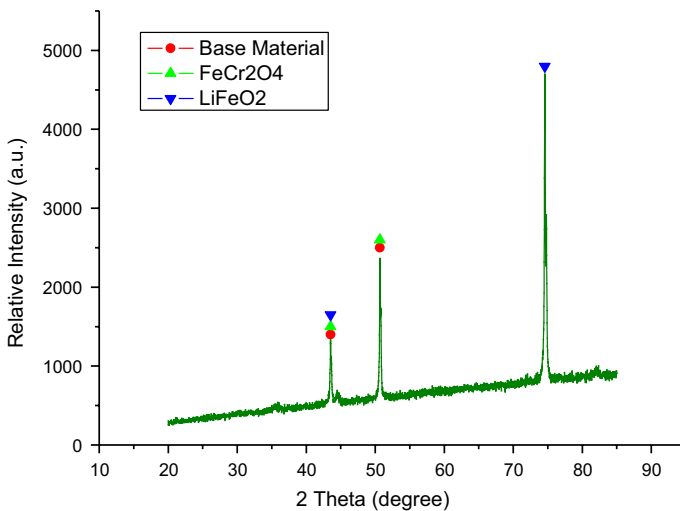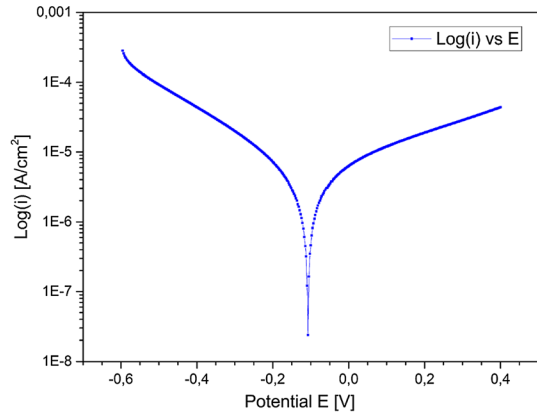Fig. 8 XRD of stainless steel 304 in $KLiNaNO_3$ at 550 °C after 600 h

Fig. 9 Polarization curves of stainless steel 304 in KLiNaNO$_3$ at 550 °C

where B is an electrochemical constant (mV) calculated theoretically and β_c and β_α are the cathodic and anodic Tafel slope, respectively, according to Eq. (5):

$$B = \frac{\beta_\alpha \cdot \beta_c}{2,3 \cdot \left(\beta_\alpha + \beta_c\right)} \tag{5}$$

The B parameter must be used to convert the R_p values into corrosion current densities, so it is necessary to make a derivation of the polarization curves as shown in Eq. (6):

$$R_p = \left.\frac{\Delta E}{\Delta i}\right|_{E=E_{corr}} = \frac{B}{i_{corr}} = \frac{\beta_\alpha \cdot \beta_c}{i_{corr} \cdot 2,3 \cdot (\beta_\alpha + \beta_c)} \tag{6}$$

The corrosion current density i_{corr} and the corrosion potential E_{corr} were determined from the extrapolation of the Tafel curve (Fig. 9). The corrosion rate (CR) can be estimated through the Faraday's law if general corrosion is assumed as observed in Eq. (7):

$$CR = \frac{i_{corr} \cdot K}{\rho_{alloy} \cdot \sum \left(\frac{f_i \cdot n_i}{MW_i}\right)} \tag{7}$$

where K is a correlation constant that defines the units of CR (3272×10^6 for CR in µm/year), ρ_{alloy} is the alloy density (g/cm^3), f_i is the mole fraction of the element i in the alloy, n_i is the number of electrons that are transferred in element i and MW_i is the atomic weight of element i.

The results obtained from the extrapolation of Fig. 9, according to Eq. 6, are shown in Table 4. The result is a corrosion rate of 5.7 µm/year obtained for 1000 h of exposure of the steel 304 in the molten salt with LiNO$_3$ content.

Table 4 Corrosion data of tested stainless steel 304 in KLiNaNO$_3$ at 550 °C

Steel	OCP (mV)	E_{corr} (mV)	j_{corr} (µA/cm^2)	CR (µm/year)	β_α (V/dec)	β_c (V/dec)
304	6.95	− 107.53	0.703	5.7	0.246	0.185

Conclusions

Electrochemical impedance spectroscopy (EIS) has been applied to monitor the corrosion behavior of a molten salt candidate that has to be applied as a thermal energy storage material for the new development of CSP plants. AISI 304 stainless steel was used for both electrochemical and static immersion tests on the ternary salt mixture consisting of 57 wt% KNO$_3$ + 13 wt% NaNO$_3$ + 30 wt% LiNO$_3$ at 550 °C for 1000 h of exposure. According to the different corrosion models available in the literature, results were fitted to the formation of a protective layer (composed of FeCr$_2$O$_4$ mainly) which has been confirmed with the SEM/EDS test and X-ray diffraction. In the same way, it is possible that the formation of LiFeO$_2$ can form a layer, which in a way works as a corrosion inhibitor.

The linear resistance polarization test was carried out at the end of experiment (1000 h) for the same steel 304, and the corrosion rate obtained presents a value of 5.7 µm/year. This result was compared with the gravimetric test with the same exposure duration of 1000 h obtaining a corrosion rate of 7.8 µm/year.

The exposed results show the great potential that EIS and linear polarization tests have for corrosion monitoring in CSP plants using molten salts as thermal energy storage material.

References

1. M. Medrano, A. Gil, I. Martorell, X. Potau and L. F. Cabeza, *Renewable and Sustainable Energy Reviews* **14**, 2010 (56–72).
2. D. Barlev, R. Vidu and P. Stroeve, *Solar Energy Materials and Solar Cells* **95**, 2011 (2703–2725).
3. Á. G. Fernández, M. Fullana, L. Calabrese, E. Proverbio, L. F. Cabeza, *Corrosion Characterization in Components for Thermal Energy Storage Applications* (2019), pp. 139–169. https://doi.org/10.1007/978-3-319-96640-3_10.
4. S. A. Kalogirou, *Solar thermal collectors and applications. Progress in Energy and Combustion Science* (2004), p, 30.
5. M. T. Islam, N. Huda, A. B. Abdullah and R. Saidur, *Renewable and Sustainable Energy Reviews* **91**, 2018 (987–1018).
6. G. McConohy and A. Kruizenga, *Solar Energy* **103**, 2014 (242–252).
7. A. G. Fernández, M. I. Lasanta and F. J. Pérez, *Oxidation of Metals* **78**, 2012 (329–348).
8. E. Brussels, O. Ce, *Concentrating Solar Power: Its Potential Contribution to a Sustainable Energy Future ea sac Building Science into EU Policy* (2011).
9. A. Gil, M. Medrano, I. Martorell, et al., *Renewable and Sustainable Energy Reviews* **14**, 2010 (31–55).

10. F. Cavallaro, E. K. Zavadskas and D. Streimikiene, *Journal of Cleaner Production* **179**, 2018 (407–416).
11. K. Kaygusuz, *Renewable and Sustainable Energy Reviews.* **15**, 2011 (808–814).
12. A. Skumanich, *Renewable Energy Focus* **11**, 2010 (40–43).
13. S. Kalaiselvam and R. Parameshwaran, *Thermal Energy Storage Technologies for Sustainability: Systems Design, Assessment and Applications. Thermal Energy Storage Technologies for Sustainability: Systems Design, Assessment and Applications*, (Elsevier, Amsterdam, 2014). https://doi.org/10.1016/c2013-0-09744-7.
14. M. Henríquez, L. Guerreiro, Á. G. Fernández and E. Fuentealba, *Renewable Energy* **149**, 2019 (940–950).
15. R. W. Bradshaw, J. G. Cordaro, N. P. Siegel, in *Proceedings of the ASME 3rd International Conference on Energy Sustainability 2009, ES2009*. American Society of Mechanical Engineers Digital Collection, vol. 2 (2009), pp. 615–624.
16. W. J. Cheng, D. J. Chen and C. J. Wang, *Solar Energy Materials and Solar Cells* **132**, 2015 (563–569).
17. R. I. Olivares and W. Edwards, *Thermochimica Acta* **560**, 2013 (34–42).
18. M. M. Bin, G. Brooks, R. M. Akbar, in *Minerals, Metals and Materials Series* (Springer International Publishing, 2017), pp. 531–539. https://doi.org/10.1007/978-3-319-51091-0_52.
19. G. Gao, F. H. Stott, J. L. Dawson and D. M. Farrell, *Oxidation of Metals* **33**, 1990 (79–94).
20. A. G. Fernández and L. F. Cabeza, *Solar Energy Materials and Solar Cells* **192**, 2019 (179–187).
21. J. R. Macdonald, *Electrochimica Acta* **35**, 1990 (1483–1492).
22. D. D. Macdonald, *Electrochimica Acta* **51**, 2006 (1376–1388).
23. G. W. Walter, *Corrosion Science* **26**, 1986 (681–703).
24. A. Kisza, *Electrochimica Acta* **51**, 2006 (2315–2321).
25. M. E. Orazem and B. Tribollet, *Electrochimica Acta* **53**, 2008 (7360–7366).
26. C. L. Zeng, W. Wang and W. T. Wu, *Corrosion Science* **43**, 2001 (787–801).
27. A. G. Fernández, A. Rey, I. Lasanta, S. Mato, M. P. Brady and F. J. Pérez, *Materials and Corrosion* **65**, 2014 (267–275).
28. A. G. Fernández and F. J. Pérez, *Solar Energy* **134**, 2016 (468–478).
29. A. G. Fernández, M. Cortes, E. Fuentealba and F. J. Pérez, *Renewable Energy* **80**, 2015 (177–183).
30. Bradshaw RW, Goods SH. Corrosion Resistance of Stainless Steels During Thermal Cycling in Alkali Nitrate. *Sandia Rep.* 2001;1–39.
31. M. C. Trent, S. H. Goods, R. W. Bradshaw, in *AIP Conference Proceedings*, vol. 1734 (American Institute of Physics Inc., 2016), p. 160017.
32. S. H. Goods, R. W. Bradshaw, M. R. Prairie and J. M. Chavez, *Corrosion of stainless and carbon steels in molten mixtures of industrial nitrates*, (Sandia National Laboratories, Albuquerque, 1994). https://doi.org/10.2172/10141843.
33. A. Mallco, C. Portillo, M. J. Kogan, F. Galleguillos and A. G. Fernández, *Applied Science* **10**, 2020 (3160).
34. M. Walczak, F. Pineda, Á. G. Fernández, C. Mata-Torres and R. A. Escobar, *Renewable and Sustainable Energy Reviews* **86**, 2018 (22–44).
35. Á. G. Fernández and L. F. Cabeza, *Solar Energy Materials and Solar Cells* **194**, 2019 (160–165).

Publisher's Note Springer Nature remains neutral with regard to jurisdictional claims in published maps and institutional affiliations.